1 Introduction

1.1 Atmospheric Chemistry

The atmosphere is composed of mostly stable gases. Over 99.9% of the gas molecules are nitrogen (78%), oxygen (21%), and argon (1%). The next three most-abundant molecules are carbon dioxide (400 ppm), methane (2 ppm), and nitrous oxide (315 ppb). All the molecules listed so far are closed-shell molecules and, as such, are relatively unreactive [1, 2].

The chemistry of the atmosphere is instead dominated by free radicals (molecules containing an unpaired electron). Despite being present in very low concentrations, these molecules are highly reactive and stimulate the majority of chemical transformation in the atmosphere. Two important families of radicals are odd-hydrogen ($HO_x = H + OH + HO_2$) and odd-nitrogen ($NO_x = NO + NO_2$). These radicals are grouped into families because they rapidly cycle between members in the atmosphere.

These families of radicals are of particular importance because of their roles in the destruction and formation of ozone. In the stratosphere, the photolysis of molecular oxygen in the ultraviolet ($\lambda < 240$ nm) produces relatively high concentrations of atomic oxygen. This atomic oxygen combines with molecular oxygen to form stratospheric ozone, but also enables HO_x and NO_x to participate in catalytic cycles that destroy ozone [2].

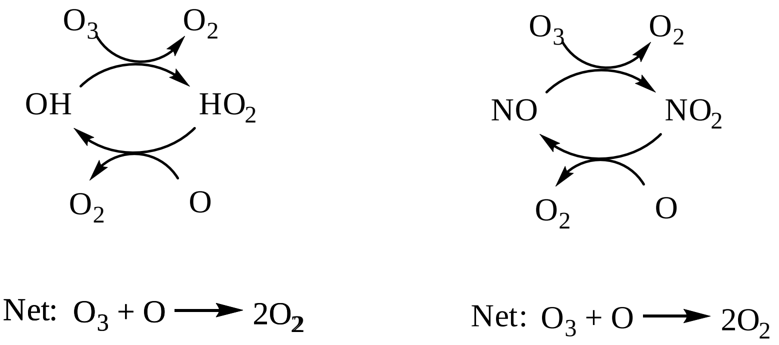

Figure 1.1. Catalytic HO_x and NO_x cycles that destroy ozone in the stratosphere.

Due to the filtering of short-wavelength ultraviolet by the stratosphere, atomic oxygen concentrations are much lower in the troposphere, and the cycles shown above do not apply. Instead, HO_x and NO_x participate in the production of ozone as a component of photochemical smog. Photochemical smog requires three chemical ingredients: hydrocarbons (RH), an oxidizer (typically OH), and NOx. A representative reaction scheme for the production of photochemical ozone is shown in Figure 1.2.

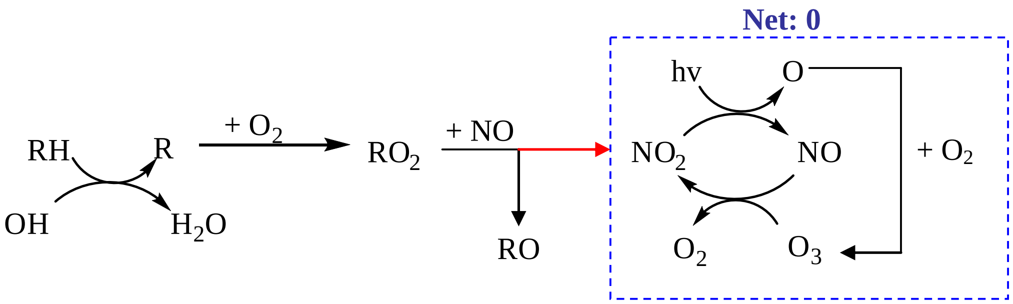

Figure 1.2. Reaction scheme for the production of tropospheric ozone.

The oxidation of hydrocarbons emitted to the atmosphere is predominantly initiated by reaction with the hydroxyl radical (OH). For unsaturated hydrocarbons, this would be hydrogen abstraction to form water and an alkyl radical (as shown in Figure 1.2); For alkenes and alkynes this would be OH addition to form a hydroxyl alkyl radical.

Alkyl radicals then add oxygen to form an alkyl peroxy radical. In the presence of NO_x, these alkyl peroxy radicals then react with NO to form NO_2 and alkoxy radicals (RO). During the daytime, NO_x in the troposphere rapidly cycles between NO and NO_2 via photolysis and reaction with O_3. This cycle (dashed box) results in no net chemical change. NO_2 produced from the reaction of NO with alkyl peroxy radicals short-circuits the normal tropospheric NO_x cycle and leads to the net production of ozone.

1.1.1 Peroxynitrous Acid

One of the most important free radical chain termination reactions is the gas phase reaction of hydroxyl radical (OH) with nitrogen dioxide (NO_2) to form nitric acid ($HONO_2$).

$$\mathrm{OH} + \mathrm{NO_2} + \mathrm{M} \xrightarrow{k_{1a}} \mathrm{HONO_2} + \mathrm{M} \qquad \text{Reaction 1.1a}$$

Reaction 1.1a sequesters reactive OH and NO_2 radicals as long-lived nitric acid, shortening their atmospheric lifetimes and slowing the catalytic cycles responsible for formation of photochemical air pollution in the troposphere and depletion of stratospheric O_3. The rate constant k_{1a} therefore affects not only HO_x and NO_x concentrations throughout the atmosphere, but also the formation of air pollutants including O_3, nitric acid, and fine particulate nitrate.

Reaction 1.1a is particularly important in polluted urban environments airsheds with high ratios of NO_x to volatile organic compounds (VOC). At high enough NO_x levels, urban ozone levels decrease with increasing NO_x, because elevated NO_x levels reduce OH concentrations through reaction 1.1a and lead to reduced VOC oxidation rates. Tonnesen [3] has shown that model predictions of ozone production can be almost inversely proportional to changes in k_{1a}. Recent sensitivity analyses have shown that modeled ozone concentrations can be more sensitive to changes in k_{1a} than changes in any other rate constant [4, 5]. The link between k_{1a} and photochemical ozone production is discussed further in appendix C.

Despite extensive studies over a wide range of temperatures and pressures, significant uncertainties remain at atmospherically relevant pressures and temperatures. Reaction 1.1a is a termolecular association reaction that requires a collision with a third body to stabilize the energetically excited initially formed complex. Such reactions can be thought of as a two-step process:

$$A + B \rightleftarrows [AB]^* \xrightarrow{M} AB\,.$$

The effective bimolecular rate constants of such reactions can be highly pressure-dependent. At very low pressures, almost every complex formed re-dissociates. The rate-limiting step to forming AB is therefore collision with a third body, and the effective bimolecular rate constant varies linearly with pressure. At very high pressures, every complex formed is immediately stabilized by a third body. As a result, the rate-limiting step is the initial formation of the AB complex and the effective bimolecular rate constant is independent of pressure. Between these two extremes, the reaction is said to be in the falloff regime and the dependence of the effective bimolecular rate constant on pressure is more complicated.

The effective bimolecular rate constant for reaction 1.1, k_1, has an anomalous fall-off curve; observed rate constants over the full range of pressures cannot be fit with a single set of falloff parameters. Robertshaw and Smith [6] first proposed that the existence of a second product channel producing peroxynitrous acid (HOONO) could explain this anomaly.

$$OH + NO_2 + M \rightarrow HOONO + M \qquad \text{Reaction 1.1b}$$

The discrepancy between the high- and low-pressure observed rate constants can be removed if the HOONO channel is insignificant at low pressures, but becomes comparable to the $HONO_2$ channel at high pressures. A significant branching fraction into channel 1.1b is of importance in the atmosphere. HOONO is less stable than nitric acid and is expected to rapidly dissociate or photolyze back to reactants. Formation of HOONO would therefore reduce the efficiency of the $OH + NO_2 + M$ reaction as a sink for OH and NO_2 radicals.

I was fortunate to participate in the first direct spectroscopic detection of HOONO and measurement of the HOONO branching ratio from reaction 1.1, k_{1b}/k_{1a} [7]. The spectra of HOONO and $HONO_2$ were measured in the mid-infrared by cavity ringdown spectroscopy. These spectra were then combined with the ratio of *ab initio* cross sections to derive k_{1b}/k_{1a} at 14 torr. These published results are included in appendix A.

The microwave discharge method used to generate OH radicals in Bean et al. limited that study to low pressures and gas mixtures of mostly H_2 and He. This left the branching ratio under conditions relevant to the lower atmosphere highly uncertain. We have since used a coupled pulsed laser photolysis/cavity ringdown apparatus to measure the pressure dependence of the reaction 1.1 branching ratio. These results are described in Chapter 3. In the process of making these new measurements, we have gained an improved understanding of the spectroscopy of both HOONO and $HONO_2$. Chapter 3 therefore also presents revisions to the results published in Bean et al.

Chapter 2 describes investigations of the spectroscopy of nitric acid. Nitric acid spectra measured in our studies of reaction 1.1 underrepresent the true nitric acid absorbance due to a cavity ringdown artifact. The main focus of Chapter 2 is a detailed analysis of this artifact to derive correction factors to be used in the branching ratio measurements. Nitric acid cross sections in the ultraviolet and infrared are also reported. These cross sections are important for researchers monitoring nitric acid concentrations either in a laboratory environment or in the atmosphere.

1.1.2 Alkoxy Radicals

Alkoxy radicals are key intermediates formed during the oxidation of hydrocarbons. Once formed, alkoxy radicals can further react via one of three pathways: decomposition, isomerization, or reaction with O_2. The end products of oxidation for a given hydrocarbon depend on the relative yield of these reaction pathways. In order to better understand the kinetics of these processes, we have studied the fate of two relatively simple alkoxy radicals, *n*-butoxy and 2-pentoxy. Chapter 5 describes the first detection of the primary isomerization products of these radicals by their infrared spectra. These spectra were then used to measure the relative rates of isomerization and reaction with O_2 for these molecules. These are the first such measurements to be made without the use of a secondary reaction product.

1.2 Experimental Technique

The atmosphere is a very complex chemical reactor. Thousands of reactions involving free radicals, photolysis, short-lived intermediates and long-lived reservoir species are constantly occurring. Our ability to understand and model this complex system depends on an accurate knowledge of the kinetics and products of individual reaction pathways. To reduce the complexity of the problem, studies of individual reactions are most easily conducted in carefully controlled laboratory experiments. The experiments described in this thesis were conducted by initiating reactions in a gas flow cell and then spectroscopically detecting products. The use of a flow cell gave us control over precursor gas concentrations and ensured that molecules detected were those of the initial products. Infrared spectroscopy enabled us to make direct and unambiguous *in situ* measurements of the products.

1.2.1 Cavity Ringdown Spectroscopy

Optical spectroscopy is one of the most powerful tools for the direct detection of gas-phase molecules. Spectroscopy relies on measuring the interaction of electromagnetic radiation with atoms or molecules. The absorbance, A, is related to the change in radiation intensity by the Beer-Lambert Law,

$$A = -\ln\left(\frac{I}{I_0}\right) = \sigma[\mathrm{X}]L, \qquad \text{Equation 1.1}$$

where I_0 and I are the light intensity before and after interacting with species X, σ is the cross section and L is the path length of the radiation through a sample with concentration [X]. The cross section is a measure of the probability a photon will be absorbed by a molecule of X and is highly dependent on the frequency of the radiation and the molecule. The variation in cross section with frequency defines a spectrum that can be used to uniquely identify molecules and quantify their concentration with eq 1.1.

The experiments described here were conducted in the mid-infrared, where spectra are predominantly due to molecular C-H and O-H stretches. These spectra provide unique fingerprints to identify molecules. The reactions we study form products in low concentrations ([x] < 0.01 torr or 10^{14} molecules×cm^{-3}) and cross sections in the infrared are typically less than 1×10^{-18} cm^2×$\mathrm{molecule}^{-1}$. Detecting products at these low concentrations therefore requires spectroscopic detection with high sensitivity. We obtain this sensitivity with cavity ringdown spectroscopy (CRDS).

CRDS is an increasingly common technique to measure absorption spectra with high sensitivity. The technique uses a high-finesse optical cavity to create very long effective path lengths and several reviews of its applications are now available [8-12]. While CRDS can be accomplished with either continuous-wave or pulsed laser sources, the discussion here will be limited pulsed CRDS systems such as ours.

In CRDS, laser light is coupled into a high-finesse optical cavity formed by two high-reflectivity ($R > 99.9\%$) mirrors. As the light travels within the cavity, the intensity gradually decreases with time due to various loss processes: transmission and scattering at the mirrors and absorption and scattering be species within the cavity.

$$I(t) = I_0 \exp\left[-\left(\#\text{ of passes}(t)\right)\times\frac{\text{loss}}{\text{pass}}\right] = I_0 \exp\left[-\frac{tc}{L_{cav}}(A+(1-R))\right] \qquad \text{Equation 1.2}$$

In eq 1.2, c is the speed of light, L_{cav} is the mirror-to-mirror length of the cavity, and it has been assumed that the dominant loss processes per pass are molecular absorption and transmission through the mirrors [13-18].

The light transmitting from the cavity at time t is proportional to the light still trapped inside the cavity. This is recorded and fit to a single exponential decay. The time it takes for the intensity to decay to I_0/e is the ringdown lifetime, τ.

$$\tau = \frac{L_{cav}}{c\left(A + \left(1 - R\right)\right)}$$

By comparing the ringdown lifetime with and without the absorber present, the Beer-Lambert absorbance can be obtained.

$$A = \frac{L_{cav}}{c}\left(\frac{1}{\tau} - \frac{1}{\tau_0}\right)$$

Due to the thousands of round-trips within the cell, the laser light interacts with the sample over very long effective path lengths (>1 km). In addition, because only the decay rate is measured, CRDS measurements are insensitive to fluctuations in laser power. As a result, per-pass absorbances smaller than 10^{-6} can be detected.

These equations only technically apply when the absorbance is constant over the linewidth of the laser. The consequences when this condition is not met are discussed in detail in Chapter 2.

1.2.2 CRDS Apparatus

Experiments were conducted in a pulsed mid-infrared CRDS spectrometer coupled to a gas flow cell. The apparatus was originally built by Garland and Fuelberth and detailed descriptions of the design and construction can be found in their theses [19, 20]. What follows is a general description of the experimental components common to all following chapters. Details such as the specific dimensions of flow cells, gas concentrations, and timing schemes are contained in experimental sections of individual chapters.

1.2.2.1 Laser System

Pulsed infrared radiation from 2.7 to 3.7 μm was produced by difference-frequency generation with an optical parametric amplifier (OPA), based on the configuration reported by Reid and Tang [21]. With typical input energies of 110 mJ of pump radiation (532 nm) and 1 mJ of signal radiation (620-660 nm), the OPA produced idler (infrared) radiation with energy $E \approx 1$ mJ/pulse, linewidth $\Gamma \approx 1$ cm^{-1} and diameter $d \approx 2$ mm after transmission through three filters to remove the residual 532 and 630 nm light. Potassium titanyl phosphate (KTP) crystals were used for the OPA because of their relatively high damage threshold (>250 MW/cm^2). The crystals were cut at 44° off the *z*-axis in the *xz* plane, with 7 mm × 7 mm crystal faces, and length of 15 mm (Crystal Technologies). Two KTP crystals were used in series in order to obtain a higher conversion of pump to signal and idler radiation and to compensate for beam displacement as the crystals were angle tuned. The angle of each KTP crystal was controlled with a stepper motor (Superior Electric Slo Syn MO61-LSO2E) mounted on a translation stage to maintain phase matching as the dye wavelength was scanned.

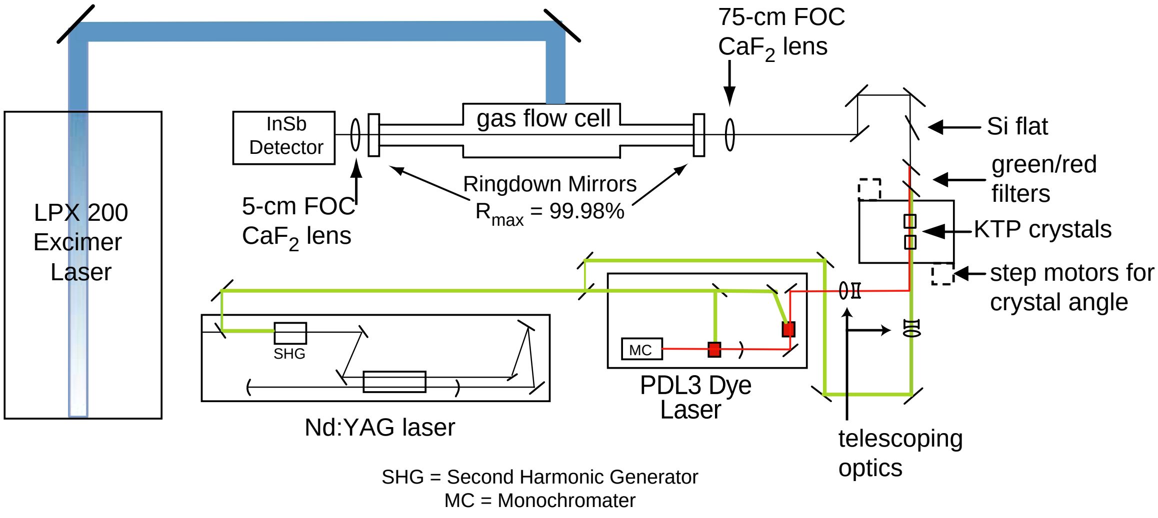

Figure 1.3. Schematic of laser system.

A schematic of the laser system and its arrangement on the laser table is shown in Figure 1.3. Schematic of laser system.Figure 1.3. The pump beam consisted of 532 nm radiation produced by doubling the output of a Nd:YAG laser (Spectra Physics GCR 130 or Continuum YG 661) operating at 10 Hz. Approximately 30% was diverted to pump a dye laser (Spectra Physics PDL3), to produce the signal radiation. The pump beam then passed through a delay line, the length of which was adjusted to optimize the temporal overlap of the pump and probe beams at the OPA. The polarization of the pump beam was then adjusted with a half-wave plate so that it entered the OPA horizontal to the plane of the laser table. The dye laser produced the signal beam with vertical polarization, and the output wavelength could be varied from 600 to 660 nm with DCM dye. Both the pump and signal beams were reduced with telescoping optics to approximately half of their original size ($d \approx 3$ mm) before being combined and sent into the OPA.

After passing through the OPA, the green and red beams were picked off with sapphire optics with antireflective coatings centered at 532 nm and 630 nm. Remaining traces of the red and green light were eliminated by passing the beams through a polished silicon optic placed at Brewster's angle (74^0) so as to allow for maximum transmission of the IR radiation. The resulting IR energy varied from 0.1 to 1.0 mJ depending on frequency. The IR radiation had a beam diameter of $d \approx 2$ mm and a linewidth of $\Gamma_L \approx 1$ cm^{-1}. The linewidth was estimated by the measured width of water and methane transitions. See chapter 2 for further discussion.

The IR beam was then sent through a series of turning mirrors to allow for alignment with the CRDS cavity. The IR beam was found to be slightly diverging, and so a 75-cm focal length CaF_2 lens was placed in front of the CRDS cell to improve coupling into the ringdown cavity. For experiments requiring UV photolysis (Chapters 3 and 4) the output of an LPX 200 excimer was aligned into the gas flow cell perpendicular to the ringdown axis.

1.2.2.2 CRDS Flow Cells

Conducting experiments in a gas flow cell provided several important benefits. Gas concentrations could be precisely determined and rapidly varied by introducing flow through calibrated flow meters. For kinetics experiments, the entire gas sample could be replaced faster than the laser repetition rate (10 Hz) to avoid the buildup and photolysis of products. Using a flow cell instead of a static gas cell also prevents the reactant and product gases from interacting with the ringdown mirrors. Due to the reactive nature of the gases used, this was critical to prevent degradation of mirror performance during the course of an experiment.

A general schematic of the flow cell system is shown in Figure 1.4. Ringdown mirrors were coupled to the gas flow cell via home-built mounts [20]. A vacuum seal is made by pressing the mirrors against O-rings. The O-rings sit in grooves machined into 2″ Conflat flanges. Fine adjustments to the mirror alignment are made by changing the position of threaded rods pressing against a washer around the outside of the mirror. The Conflat flanges with mounted mirrors are then attached to another pair of Conflat flanges fixed to the laser table. The first of these flanges has a feedthrough for inert purge gas (Ar or N_2). The second flange was welded to a ¾″ Ultratorr adapter used to connect the mirror mount assembly to the gas flow cell.

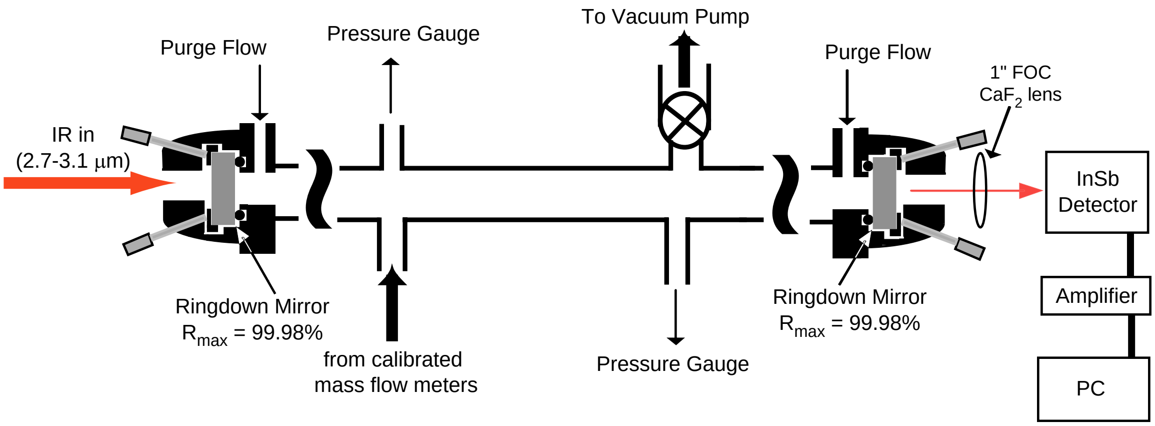

Figure 1.4. Diagram of CRDS-coupled gas flow cell.

Gas flow cells of various dimensions and materials were used. In addition to connectors on the ends to couple to the mirror mounts, all cells used had at least three ports: one for the input of reactant gas mixtures, one for the pumping out of the cell, and one for measuring the cell pressure. Most cells had a second port for measuring pressure so that pressure gradients within the cell could be quantified. All gases were flowed through calibrated mass flow meters and then mixed prior to entering the cell. The cell was pumped by high-throughput mechanical pumps to facilitate the rapid flushing of the cell. The pressure in the cell was controlled by adjusting a valve between the cell and the vacuum line.

1.2.2.3 CRDS Measurements

Because of the large losses at the mirrors, measuring the infrared radiation leaking from the CRDS cavity required a sensitive detection method. The ringdown cavity output was tightly focused with a 1″-focal length CaF_2 mirror onto the sensor of a liquid nitrogen-cooled InSb photodiode (Judson Technologies J10D-M204-R01M-60). Accurate measurements of ringdowns require a fast detector, so a photodiode with a small (1 mm) active area was used. The detector was then amplified, filtered to reduce high-frequency noise, and digitized.

Each ringdown trace was amplified and then accumulated with a 50 MHz bandwidth digital oscilloscope card with 14-bit digitizer (GageScope 1450). For each point in a spectrum, 16 ringdown traces were averaged and fit to a single-exponential function and constant baseline by a nonlinear Levenberg-Marquardt algorithm. Due to noise in the ringdowns at early times, the earliest part of the recorded decays was removed before fitting. This was accomplished by making an initial log-linear fit to estimate the lifetime, then cutting data points corresponding to the first half lifetime before the decay was fit with the Levenberg-Marquardt algorithm. The first half lifetime was cut from each decay before fitting. Scanning of the OPA system, collection of the spectra, and the fitting of accumulated ringdown traces were controlled by a Labview PC program.

The CRDS mirrors (Los Gatos Research), with R=99.98%, have their maximum reflectivity at 2.8 μm. Typical background ringdown times were about 7 μs and about 5 lifetimes are collected and fit at 50 MSamples s^{-1}. The quality of the single-exponential fits depended on the alignment of the optical cavity, the alignment of the IR beam into the cavity, and the alignment of the focused IR output on the detector active area. As a result, the shot-to-shot fitting variance in the measured empty cell ringdown lifetime varied over the range $\Delta\tau/\tau = 0.3\% - 2.0\%$. For a typical cavity length of L_{cav} = 50 cm ($1/\tau$ = 120,000) this corresponds to a minimum detectable absorbance of 0.6–2 ppm averaging 16 shots or 0.75-5.0 ppm $Hz^{-1/2}$.